Research paper

# Synthesis of Bi$_2$O$_3$@BiOI@UiO-66 composites with enhanced photocatalytic activity under visible light

Jijun Tang [a], Tang Zhang [a], Zhengzhou Duan [a], Chuwen Li [a], Chunfeng Meng [a], Yamei Zhang [a], Qiyuan Zhang [b], Dongmei Hou [b], Qinyun Xv [b], Yu Zhu [b,*,*]

[a] School of Materials Science and Engineering, Jiangsu University of Science and Technology, Zhenjiang 212003, PR China
[b] Taizhou University, College of Pharmacy and Chemistry & Chemical Engineering, Jiangsu Key Laboratory of Chiral Pharmaceuticals Biomanufacturing, Taizhou 225300, PR China

ARTICLE INFO

ABSTRACT

Bi$_2$O$_3$ is a photocatalyst with excellent performance; however, its applications are limited due to its wide bandgap. In this paper, by adding BiOI and the metal–organic framework UiO-66, a Bi$_2$O$_3$@BiOI@UiO-66 composite material is obtained with high adsorption capacity, in which the bandgap of Bi$_2$O$_3$ is reduced, the recombination of photogenerated electrons and holes is prevented, the photocatalytic efficiency and stability are improved. In visible light degradation experiments, Bi$_2$O$_3$@BiOI@UiO-66 has obvious degradation effects on Rhodamine B and tetracycline, which are 22.2 and 1.04 times that of pure Bi$_2$O$_3$, respectively. Bi$_2$O$_3$@BiOI@UiO-66 demonstrats its potential as photocatalytic degradation material.

## 1. Introduction

With the development of social industrialisation, persistent organic pollutions (POPs) are increasingly contaminating water resources [1,2]. In this context, photocatalytic technologies have been receiving considerable attention because they can efficiently degrade POPs to harmless molecules such as H$_2$O and CO$_2$ on the basis of the redox ability of the photocatalyst upon light irradiation [3]. Bi$_2$O$_3$ is a promising candidate in this regard due to its high electrochemical stability and high redox reversibility [4,5]. However, the wide application of pure Bi$_2$O$_3$ is still constrained due to its wide bandgap. BiOX (X = Cl, Br and I) semiconductors having a layered inner structure can accelerate the separation efficiency of photogenerated carriers for high photocatalytic activity because of the built-in electric field; therefore, they have emerged as new efficient and environmental-friendly photocatalytic materials [6]. In particular, BiOI has a narrow bandgap (1.63–2.20 eV) [7] that provides it with excellent photocatalytic performance under visible light irradiation. In fact, the combination of BiOI with Bi$_2$O$_3$ can effectively reduce the bandgap of the latter, facilitating the generation of electrons under visible light [8–13]. However, photogenerated electrons and holes can be easily recombined, resulting in a decrease in photocatalytic efficiency [14,15].

The combination of semiconductor materials and metal–organic framework (MOF) materials has proved effective to solve this problem [16]. MOFs are a class of crystalline porous materials with periodic network structures formed by the self-assembly of inorganic metal centres (metal ions or metal clusters) and bridged organic ligands, affording a specific surface area that increases the contact area and improves the photocatalytic efficiency [17]. As an example of MOF, thermally and chemically stable UiO-66 has been applied in various fields including liquid separation, adsorption and catalysis [18,19]. The addition of UiO-66 to composite materials improves the transfer pathway of photogenerated electron and holes, thereby reducing the recombination of electrons and valence band holes. Therefore, the catalytic efficiency is improved in composites containing porous UiO-66 [20–26].

Following this line of thought, we were interested in evaluating the effect of the addition of UiO-66 on the photocatalytic activity of the Bi$_2$O$_3$@BiOI systems. In this paper, Bi$_2$O$_3$@BiOI binary composite materials and Bi$_2$O$_3$@BiOI@UiO-66 ternary composite materials were synthesised by an improved solvothermal method. The optimal substrate ratio in the composites was determined, and the porous structure of the MOF material was found to improve the photocatalytic efficiency of the binary system, providing a method for the degradation of organic dyes.

## 2. Experimental

### 2.1. Synthesis of $Bi_2O_3$

As reported in a previous work [27], $Bi_2O_3$ was synthesised using $Bi_2O_2CO_3$ as a precursor. First, 11.64 g of $Bi(NO_3)_3 \cdot 5H_2O$ was dissolved in 60 mL of $HNO_3$ aqueous solution (1 mol/L). To this mixture, 240 mL of $Na_2CO_3$ aqueous solution (0.6 mol/L) was slowly added with constant stirring, resulting in the formation of a large amount of a white precipitate. The suspension was further stirred for 15 min and left to stand at 60 °C for 12 h. Finally, the precipitate was collected, washed several times with deionised water and dried at 60 °C for 6 h to form the $Bi_2O_2CO_3$ precursor. $Bi_2O_3$ was obtained by annealing the as-prepared $Bi_2O_2CO_3$ at 350 °C for 30 min.

### 2.2. Synthesis of UiO-66

Following a reported procedure [28], 0.233 g of $ZrCl_4$ and 0.166 g of $H_2BDC$ were dissolved in 50 mL of DMF with stirring for 30 min and then reacted at 120 °C for 24 h in a hydrothermal reaction vessel. The resulting product was washed and dried at 80 °C for 12 h.

### 2.3. Synthesis of $Bi_2O_3$@BiOI

Different ratios of $Bi_2O_3$ and 1 mmol of $Bi(NO_3)_3 \cdot 5H_2O$ were added to a solution containing 1 g of KI in ethylene glycol, mixed thoroughly, placed in a hydrothermal reaction kettle and reacted at 110 °C for 24 h. After cooling to room temperature, the mixture was washed with water and ethanol, then dried at 80 °C.

### 2.4. Synthesis of $Bi_2O_3$@BiOI@UiO-66

UiO-66, $Bi_2O_3$ and 1 mmol of $Bi(NO_3)_3 \cdot 5H_2O$ were added to a solution containing 1 g of KI in ethylene glycol (2.5 mL), mixed thoroughly and placed in a hydrothermal reaction kettle. The reaction was conducted at 110 °C for 24 h. Then, the mixture was cooled to room temperature, washed with water and ethanol and dried at 80 °C.

### 2.5. Characterisation

X-ray diffraction (XRD) data were collected on a Shimadzu XRD-6000 instrument. Scanning electron microscopy (SEM) was performed on a Japan Electronics JSM-6480 microscope to observe the morphology of the photocatalysts. Fourier transform infrared (FTIR) spectra were obtained using an Agilent spectrometer in a frequency range of 4500–450 $cm^{-1}$. The absorption spectra were recorded on a Hitachi U4100 UV spectrometer. $N_2$ physisorption measurement was performed at 77 K on a BELSORP-mini II instrument; each sample was degassed in vacuo at 200 °C for 3 h. The specific surface area was determined according to the Brunauer-Emmett-Teller (BET) equation. Fluorescent spectra were obtained on a FS5 spectrofluorometer. The transient photocurrent measurements were performed using an Electrochemical Workstation (Chenhua 660E, China), equipped with three-electrodes involving ITO electrode covered with samples, Pt and Ag/AgCl electrodes. For the single working electrode, 5 mg of the sample was dispersed in 10 μL nafion and then added 0.1 mL anhydrous ethanol to make a homogeneous solution. Then, 40 μL of above solution was dropped on ITO conducting glass. The 0.5 M $Na_2SO_4$ aqueous solution was used as the electrolyte and exposed by Xe lamp (300 W, λ > 420 nm). The impedance test is performed in the frequency range of 0.1 Hz–10 kHz, an amplitude of 0.005 V, a Quiet time of 2 s, and an initial potential of 0.071 V.

### 2.6. Photocatalytic activity test

The photocatalytic degradation of Rhodamine B (RhB) and tetracycline (TC) by the prepared samples ($Bi_2O_3$@BiOI and $Bi_2O_3$@BiOI@UiO-66) was studied under visible light irradiation. A 250 W Xe lamp (λ ≥ 420 nm) with an ultraviolet cut-off filter was used as the visible light source. The photocatalyst (20 mg) was dispersed in a 100 mL aqueous solution of RhB (10 mg/L) and stirred in the dark for 30 min to form an adsorption–desorption system. After centrifuging the suspension to remove the catalyst from the aqueous solution, the absorbance of RhB or TC was analysed by a 759 UV–vis spectrophotometer. Benzoquinone (BQ), sodium oxalate ($Na_2C_2O_4$) and isopropanol (IPA) were used as a superoxide anion ($\cdot O_2^-$) scavenger, a hole (h) scavenger and a hydroxyl radical scavenger ($\cdot OH$) respectively.

## 3. Results and discussion

### 3.1. Morphology and structure

The crystal structure and phase composition of the samples were determined by powder XRD (Fig. 1). The major characteristic peaks of the $Bi_2O_3$ sample at around $2\theta = 28.01°$, 33.25° and 46.37° could be readily indexed to monoclinic α-$Bi_2O_3$ according to the standard card JCPDS NO. 71–2274 and were ascribed to the $(-1\,2\,1)$, $(-2\,0\,2)$ and $(0\,4\,1)$ lattice planes, respectively [29]. The four major peaks of BiOI at $2\theta = 29.7°$, 31.7° and 55.2° were assigned to the $(1\,0\,2)$, $(1\,1\,0)$ and $(2\,1\,2)$ planes, illustrating that the synthesised BiOI has a tetragonal phase (JCPDS NO. 10-0445) [30]. The patterns of the $Bi_2O_3$@BiOI composites show all the peaks of BiOI but not those of $Bi_2O_3$. This may be due to the overlapping of the BiOI peaks at 46.37° and 55.2° with the $Bi_2O_3$ peaks having weak intensity of diffraction. The characteristic peaks of UiO-66 located at $2\theta = 7–9°$ are in line with previous reports, suggesting that UiO-66 crystals were successfully synthesized [17,31]. In the $Bi_2O_3$@BiOI@UiO-66 sample, the peaks at 7° and 9° are much smaller than those of pure UiO-66, which may be because $Bi_2O_3$@BiOI covers the crystal plane of UiO-66 during the formation of the composite.

The morphology of the substrates $Bi_2O_3$, BiOI and UiO-66 (Fig. 2) and the $Bi_2O_3$@BiOI and $Bi_2O_3$@BiOI@UiO-66 composites (Fig. 3) was characterised using SEM. As can be seen in Fig. 2a, $Bi_2O_3$ displays a hollow rod-like structure with a particle size of 20–30 μm and an inner pore diameter of 5 μm. BiOI is a cluster of flower-shaped aggregates with a diameter of about 2 μm (Fig. 2b). Fig. 2c shows the octahedral crystal structure of UiO-66 with a diameter of 600 nm. As can be extracted from the SEM images of the composites (Fig. 3), the top smaller rod-shaped load material is $Bi_2O_3$, which is relatively evenly distributed on BiOI (Fig. 3a–c). Fig. 3d shows that the regular holes of UiO-66 are loaded
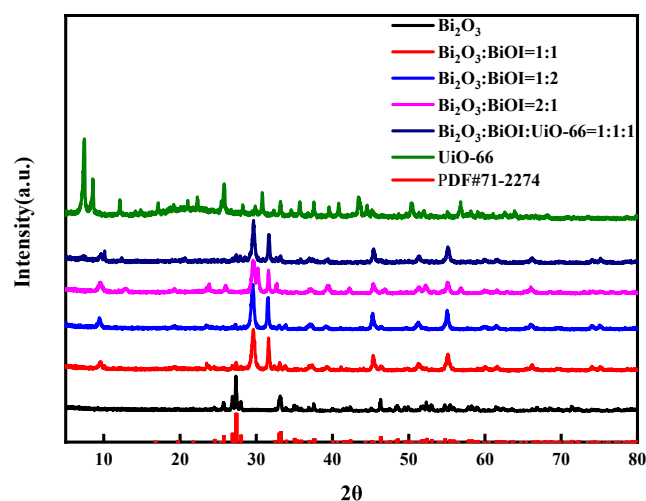


**Fig. 1.** X-ray diffraction spectra of $Bi_2O_3$@BiOI and $Bi_2O_3$@BiOI@UiO-66 prepared with different substrate ratios.

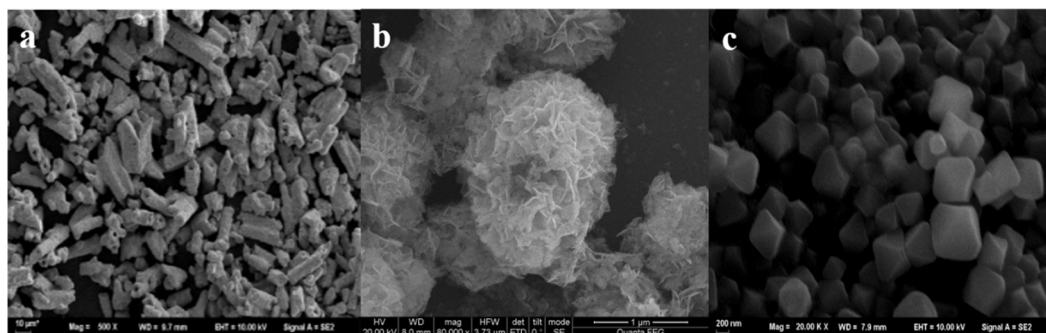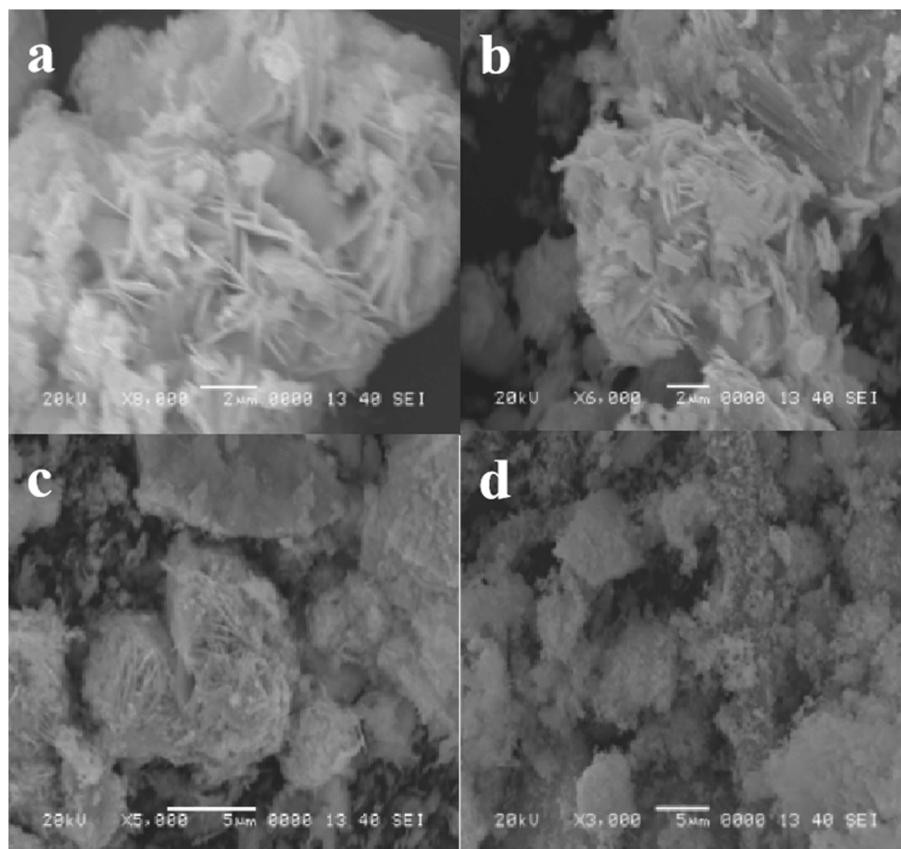**Fig. 2.** Scanning electron microscopy images of (a) $Bi_2O_3$, (b) BiOI and (c) UiO-66.



**Fig. 3.** Scanning electron microscopy images of (a), (b), (c) the $Bi_2O_3$@BiOI binary composite at three different substrate ratios (1:1, 1:2, 2:1), and (d) the $Bi_2O_3$@BiOI@UiO-66 ternary composite.

with flower-like and rod-shaped substances, which confirms that $Bi_2O_3$ and BiOI were successfully loaded onto UiO-66.

Infrared spectroscopy verified the each peak of UiO-66 and composite materials. (Fig. S1) The sharp peak observed at 530 cm$^{-1}$ can be assigned to the typical stretching modes of Bi–O [17,31]. The presence of $Bi_2O_3$ was confirmed by the band at 423 cm$^{-1}$, which is attributable to the symmetrical stretching vibration of the Bi–O bond of $Bi_2O_3$ species [32,33]. The peak at 744 cm$^{-1}$ likely originates from the O–Zr–O vibration of UiO-66, and small peaks located in the range 700–1200 cm$^{-1}$ stem from the vibration of aromatic rings. The presence of three strong peaks at 1392, 1590 and 1670 cm$^{-1}$ attributed to carboxyl groups of the ligands is in accord with previous reports [34–36].

BET was used to characterise the specific surface area and pores of UiO-66 [30] and the composite materials [17]. The specific surface area of UiO-66 is about 794.69 m$^2$ g$^{-1}$, whereas that of the $Bi_2O_3$@BiOI @UiO-66 composite is 51.14 m$^2$ g$^{-1}$ (Table S1 and Fig. 4). In addition,

the pore size of pure UiO-66 (2.232 nm) is smaller than that of the composite (3.206 nm). However, the specific surface area of the composite material is still much larger than that of $Bi_2O_3$ (8.149 m$^2$ g$^{-1}$) [37,38]. This result demonstrates that the addition of UiO-66 improves the specific surface area of the final product compared with the $Bi_2O_3$ substrate.

The as-prepared $Bi_2O_3$, BiOI and composite materials were shown in the UV–vis diffuse reflectance spectra (Fig. S2). According to the Kubelka–Munk curve and the fitting of the spectrum, the forbidden bandwidth of $Bi_2O_3$ is 2.7 eV, whereas those of $Bi_2O_3$@BiOI and $Bi_2O_3$@BiOI@UiO-66 are 1.89 and 1.94 eV, respectively (Fig. S2b, S2c). Due to this reduction of the bandgap in the composites, electrons are more easily excited into photogenerated electrons in solution to participate in the photocatalytic reaction, which improves the photocatalytic degradation efficiency of the material.

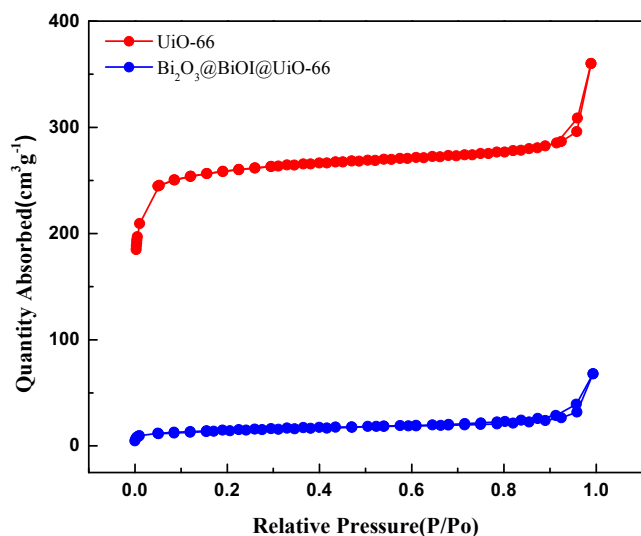To further confirm the effective charge separation in the materials,

**Fig. 4.** $N_2$ adsorption and desorption isotherms.

the samples were measured by fluorescence spectroscopy with an excitation wavelength of 530 nm. An emission peak is observed around 648 nm, which originates from the recombination of photogenerated electrons and valence band holes (Fig. 5). The peak intensity of $Bi_2O_3$ is five times that of $Bi_2O_3@BiOI$ and $Bi_2O_3@BiOI@UiO-66$. The lower emission intensity for the composites indicates that they are more conducive to charge separation, thereby inhibiting the recombination of electron–hole pairs [39].

### 3.2. Photocatalytic performance

We evaluated the catalytic degradation ability of pure $Bi_2O_3$ and the $Bi_2O_3@BiOI$ and $Bi_2O_3@BiOI@UiO-66$ samples using RhB and TC as pollutants under visible light irradiation. The experiment was repeated three times to get the variance and shown on the chart. (Fig. 6) The following first-order kinetic formula was used to fit the experimental data: $\ln(C_0/C) = kt$, where $C_0$ and $C$ are the concentrations of pollutants in the solution at times 0 and t, respectively, and $k$ is the photocatalytic rate constant.

First, the photocatalytic performance of the $Bi_2O_3@BiOI$ and $Bi_2O_3@BiOI@UiO-66$ composites in the degradation of RhB was assessed. In the dark, $Bi_2O_3@BiOI@UiO-66$ exhibited the best RhB
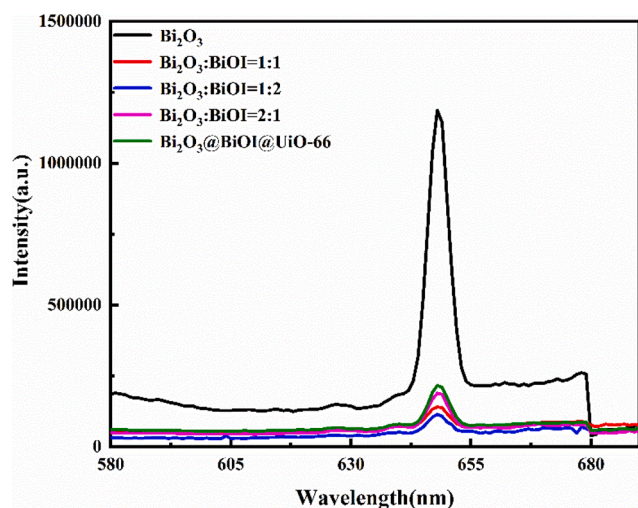


**Fig. 5.** Emission fluorescence spectra of $Bi_2O_3$ and the binary and ternary composite materials.

adsorption effect, whereas that of $Bi_2O_3@BiOI$ was basically the same as that of $Bi_2O_3$. Due to the large specific surface area of UiO-66, the $Bi_2O_3@BiOI@UiO-66$ composite can absorb more RhB molecules than the binary composite. The degradation rate of $Bi_2O_3@BiOI@UiO-66$ reached an astonishing 89.9% when exposed to visible light (Fig. 6a). After first-order kinetics fitting, the $k$ value of $Bi_2O_3@BiOI@UIO-66$ was found to be the largest ($k = 0.03437$ min$^{-1}$), and those of the other materials followed the order $Bi_2O_3 > 0.5Bi_2O_3@BiOI > 2Bi_2O_3@BiOI > 1Bi_2O_3@BiOI$ (Fig. 6b). Due to the narrow bandgap of BiOI, $Bi_2O_3$ not only produces photogenerated electrons more easily upon visible light irradiation but also improves their mobility [40]. The recombination of photogenerated electrons and holes in $Bi_2O_3@BiOI$ is hindered by adding UiO-66, and $Bi_2O_3@BiOI@UiO-66$ has high adsorptivity. This results in multiple reaction centres on the surface of the material, thereby improving the photocatalytic efficiency.

TC has also been selected as a pollutant to study the photocatalytic activities of these materials. In dark, the adsorption capacity of $Bi_2O_3@BiOI@UiO-66$ increased to a certain extent via composited with UiO-66 compared with $Bi_2O_3$, BiOI and $Bi_2O_3@BiOI$. The degradation rate of TC by $Bi_2O_3@BiOI@UiO-66$ was 63.6% when exposed to visible light, and the degradation rate of $Bi_2O_3$ turned out to be 60.1% (Fig. 6c). The $k$ value of $Bi_2O_3@BiOI@UiO-66$ was still the largest ($k = 0.00974$ min$^{-1}$), and those of the other samples followed the order $Bi_2O_3 > 2Bi_2O_3@BiOI > 1Bi_2O_3@BiOI > 0.5Bi_2O_3@BiOI$ (Fig. 6d). The high degradation rate of $Bi_2O_3$ may be due to the large adsorption of TC in the dark.

Besides, the adsorption also acts as an important part for the pollutant removing. UiO-66 has a specific surface area of 794.69 m$^2 \cdot$g$^{-1}$, which can improve the adsorption performance of semiconductors. In photocatalytic process, $Bi_2O_3@BiOI@UiO-66$ can enrich pollutants with low concentration around or on UiO-66 due to the good adsorption capacity. Compared with $Bi_2O_3$, $Bi_2O_3@BiOI$, $Bi_2O_3@BiOI@UiO-66$ exhibited the best adsorption effect on the two pollutants. Because of the different sizes of pollutants, the adsorption to TC with 37% in dark is a little larger than that to RhB which owns a larger size with 23%.

Photogenerated holes, $\cdot OH$, $\cdot O_2^-$ are important active substances for photodegradation. The degradation of organic matter is dominated by free radical redox reactions. In the degradation of RhB, the addition of isopropanol has the greatest impact on photodegradation, which proves that the degradation of RhB is dominated by $\cdot OH$ (Fig. 7a). Besides, benzoquinone has the greatest impact on the photodegradation of TC, indicating $\cdot O_2^-$ the primary factor in the photodegradation of TC (Fig. 7b). Furthermore, EPR was measured here to distinguish the free radicals with DMPO as the scavenger [41,42]. A characteristic quartet signal for DMPO-$\cdot O_2^-$ and $\cdot OH$ with an intensity ratio of approximately 1:1:1:1 is observed in Figs. 8 and 9, confirming the generation of $\cdot O_2^-$ and $\cdot OH$ over the $Bi_2O_3@BiOI@UiO-66$ catalyst under visible light irradiation.

The photocatalytic degradation of RhB by $Bi_2O_3@BiOI@UiO-66$ was compared in different pH (Fig. S3a, S3b) and solutions containing different ions (Fig. S3c, S3d). It is basically unaffected in acidic solutions and the photocatalytic performance of the sample on RhB also varies slightly with good stability in solutions with different ions. The photocatalytic degradation of tetracycline by $Bi_2O_3@BiOI@UiO-66$ was also compared in different pH (Fig. S4a, S4b) and solutions containing different ions (Fig. S4c, S4d). It is found that the photocatalytic performance of the sample has a certain downward trend in different pH and different ions, but the photocatalytic efficiency can still be maintained. The degradation of the RhB has been carried out five runs to test the stability (Fig. S5). The degradation ratio is decreasing from 88.9% to 83.9%, which is only about 5% loss in RhB degradation (Fig. S5). Besides, $Bi_2O_3@BiOI@UiO-66$ was tested by XRD to confirm the stability before and after photocatalysis. The peaks remain unchanged, which shows that $Bi_2O_3@BiOI@UiO-66$ can still maintain the complete structure after photocatalysis with no changes in components (Fig. S6).

To study the carriers transfer process and separation process in photocatalysts, the photoelectrochemical analyses were performed.
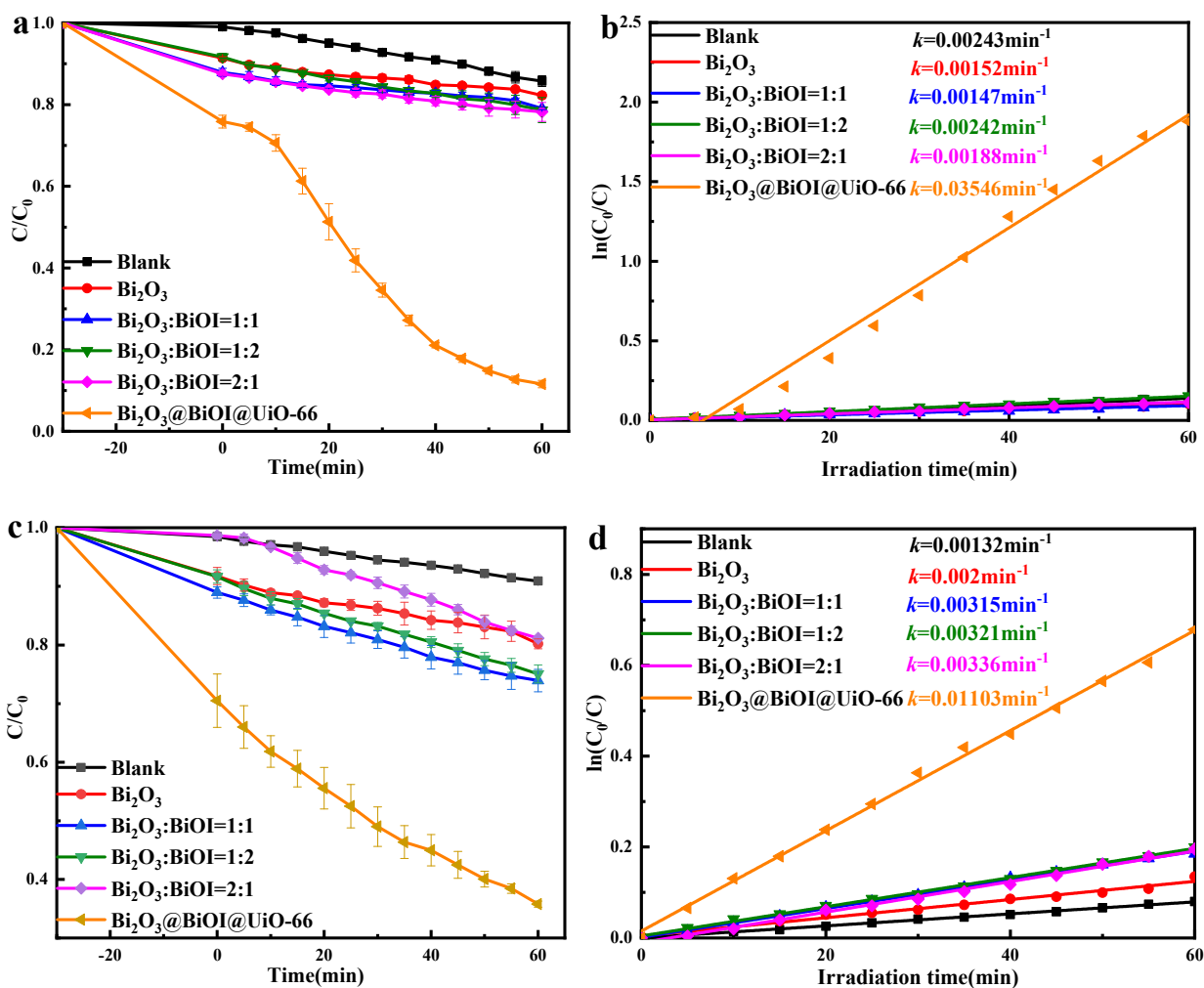
**Fig. 6.** (a) and (b) Degradation efficiency and fitting rate constant of RhB (10 mg/L) by different samples; (c) and (d) Degradation efficiency and fitting rate constant of TC (10 mg/L) by different samples.
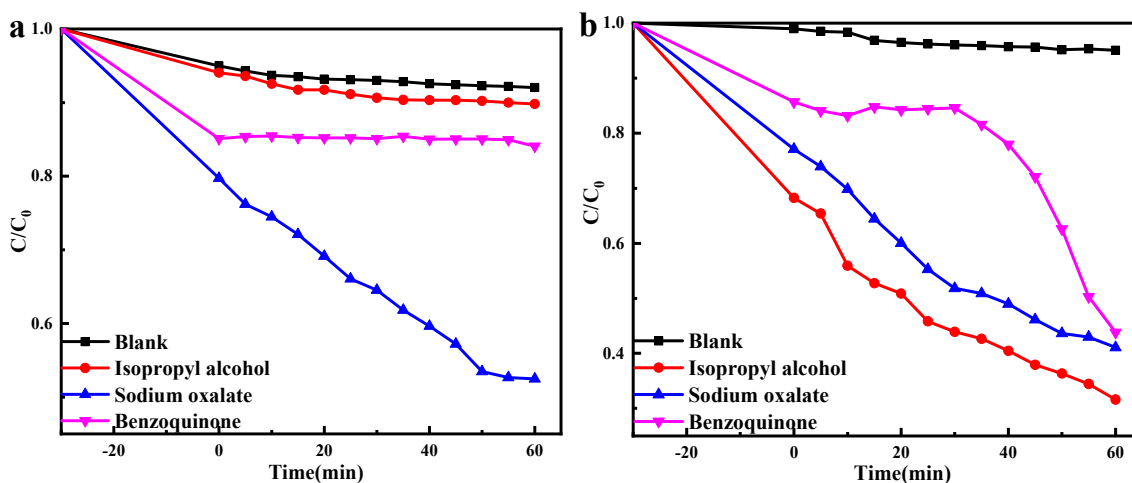


**Fig. 7.** Photocatalytic degradation rate of RhB (a) and TC (b) in different inhibitors.

Compared with $Bi_2O_3$, BiOI and $Bi_2O_3@BiOI$, $Bi_2O_3@BiOI@UiO-66$ displays the strong photo current response, revealing the efficient photo-induced charge transfer between $Bi_2O_3$, BiOI and UiO-66 (Fig. 10). The superior charge transfer and recombination inhibition in $Bi_2O_3@BiOI@UiO-66$ is responsible for the intensive photocatalytic activity

[43]. To further confirm above results, EIS Nyquist plot for monomer and composite materials has been used to study the course of charge separation and transfer. Fig. 11 displays the Nyquist impedance plots of monomer and composite materials. The resistance $R_{ct}$ value of each sample is BiOI(16.23 Ω) > $Bi_2O_3$(16.13 Ω) > $Bi_2O_3@BiOI$(14.97 Ω) >
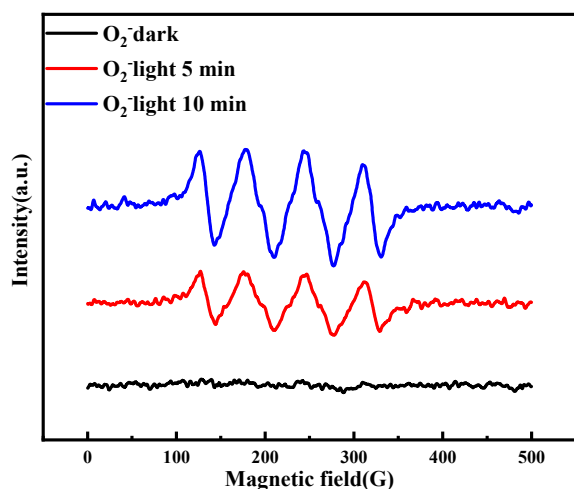
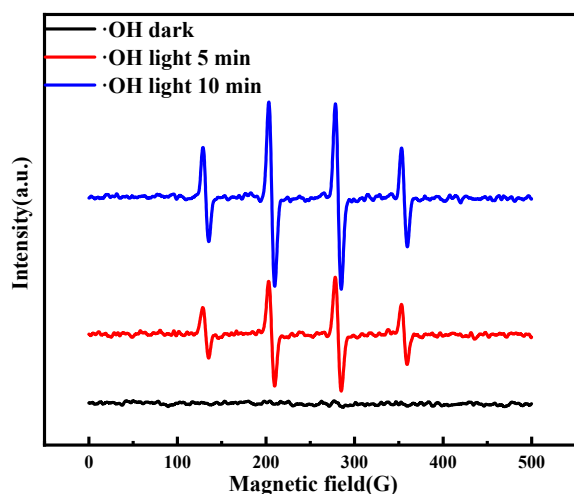**Fig. 8.** EPR spectra in methanol dispersion for DMPO-·$O_2^-$.



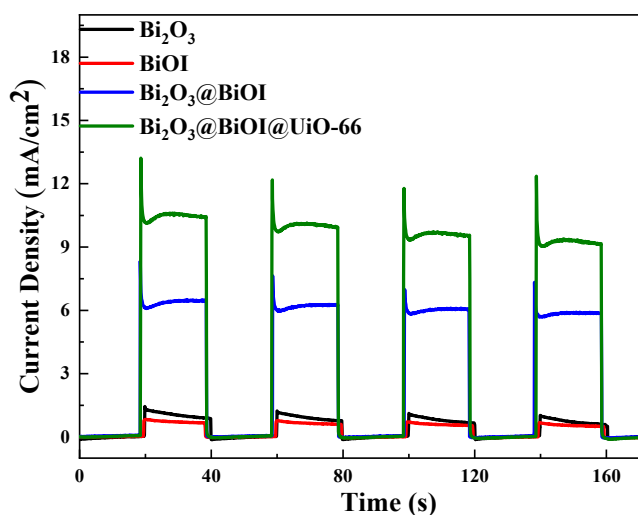**Fig. 9.** EPR spectra in methanol dispersion for DMPO-·OH.



**Fig. 10.** Photocurrent response graph of monomer, binary composite and ternary composite (electrolyte composition: 0.5 M $Na_2SO_4$, electrode area: 1 $cm^2$, optical power: 300 W).
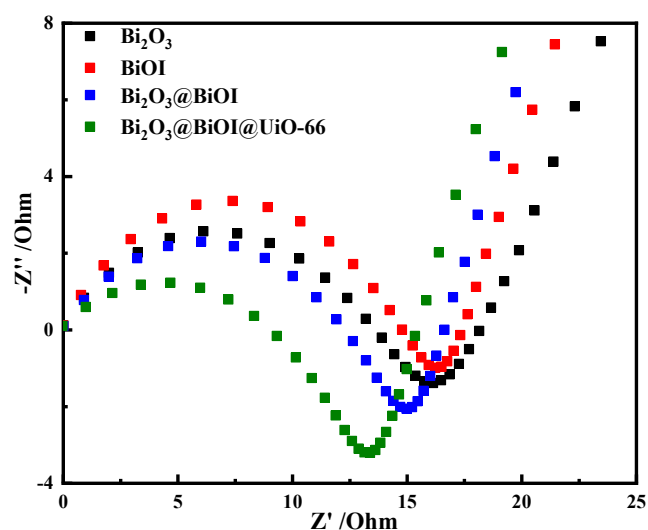


**Fig. 11.** Nyquist plots in the 0.5 M $Na_2SO_4$ solution, 0.01 Hz to 10 kHz frequency range, Initial potential 0.071 V, 0.005 V amplitude, 2 sec quiet time 0.5 M $Na_2SO_4$ for the electrodes.

$Bi_2O_3$@BiOI@UiO-66(13.42 Ω), while the capacitance C is BiOI(0.94 C) > $Bi_2O_3$@BiOI(0.90 C) > $Bi_2O_3$(0.89 C) > $Bi_2O_3$@BiOI@UiO-66(0.93 C).(Fig. S7) What's more, the |Z| value of different samples does not change greatly with the increase of frequency, which proves the stability of the samples to the circuit signal. Compared with $Bi_2O_3$, the phase angle changes are concentrated in the low frequency region, which proves that the material's response to the circuit is mainly in the low frequency region and the capacitive reactance arc is smaller than $Bi_2O_3$. This reflects that $Bi_2O_3$@BiOI@UiO-66 is more polarized larger, higher current discharge capability is better. It is found that $Bi_2O_3$@BiOI@UiO-66 displays a low arc radius in comparison to other samples, suggesting that $Bi_2O_3$@BiOI@UiO-66 owns strong migration and separation of photo-generated charge carrier.

From the photocatalytic experiments, it can be extracted that the interaction between BiOI, $Bi_2O_3$ and UiO-66 is responsible for the efficient generation and separation of carriers under visible light excitation (Fig. 12). For a semiconductor, at the point of zero charges, the band positions can be calculated by the following empirical formula:
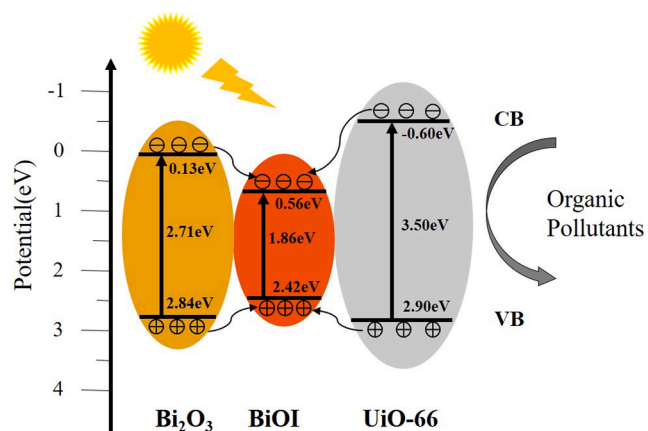
$$E_{VB} = X - Ee + 0.5Eg$$

$$E_{CB} = E_{VB} - E_g$$



**Fig. 12.** Energy band structure and charge separation map of materials, and possible ways of photodegradation of pollutants.

where $E_{VB}$ and $E_{CB}$ are the valence band (VB) and conduction band edge potentials, respectively, and X is the electronegativity of the semiconductor, which is the geometric mean of the electronegativity of the constituent atoms [44]. BiOI, with a narrow bandgap energy of 1.86 eV, could be easily excited by visible light ($\lambda > 400$ nm, energy less than 3.10 eV), inducing the generation of electrons and holes. After $Bi_2O_3$@BiOI@UiO-66 is irradiated with visible light, because BiOI has the lowest conduction band, electrons are excited on BiOI to form photoinduced carriers, which are then transferred from BiOI to $Bi_2O_3$ and UiO-66 and released [45].

## 4. Conclusion

In this paper, a solvent method was used to synthesise $Bi_2O_3$@BiOI and $Bi_2O_3$@BiOI@UiO-66 composites with different substrate ratios as photocatalysts to degrade RhB and TC under visible light irradiation. The degradation rate of $Bi_2O_3$@BiOI@UiO-66 for RhB and TC is six and three times that of the $Bi_2O_3$@BiOI system, respectively. The results show that addition of UiO-66 increases significantly the adsorption capacity of the sample, accelerates the charge separation and reduces the electron–hole recombination during the photocatalytic process. In addition, $Bi_2O_3$@BiOI@UiO-66 shows good stability. Therefore, the high efficiency and stability of the $Bi_2O_3$@BiOI@UiO-66 composite renders it a good candidate material for photocatalytic applications.

## CRediT authorship contribution statement

**Jijun Tang:** Supervision, Writing - original draft, Data curation. **Tang Zhang:** Investigation, Writing - original draft, Software. **Zhengzhou Duan:** Software. **Chuwen Li:** Formal analysis. **Chunfeng Meng:** Resources. **Yamei Zhang:** Resources. **Qiyuan Zhang:** Methodology. **Dongmei Hou:** Investigation. **Qinyun Xv:** Investigation. **Yu Zhu:** Supervision, Project administration, Writing - review & editing.

## Declaration of Competing Interest

The authors declare that they have no known competing financial interests or personal relationships that could have appeared to influence the work reported in this paper.

## Acknowledgement

## Appendix A. Supplementary material

Supplementary data to this article can be found online at https://doi.org/10.1016/j.cplett.2021.138354.

## References

[1] X. Qian, D. Yue, Z. Tian, M. Reng, Y. Zhu, M. Kan, T. Zhang, Y. Zhao, Carbon quantum dots decorated $Bi_2WO_6$ nanocomposite with enhanced photocatalytic oxidation activity for VOCs, Appl. Catal. B-Environ. 193 (2016) 16–21.

[2] Z. Zhang, J. Zhang, S. Li, J. Liu, M. Dong, Y. Li, N. Lu, S. Lei, J. Tang, J.J.C. Fan, Effect of graphene liquid crystal on dielectric properties of polydimethylsiloxane nanocomposites, Compos. Part B: Eng. 176 (2019) 107338.

[3] S. Ghanbari, M.H. Givianrad, P.A. Azar, Synthesis and characterization of visible light driven N—Fe-codoped $TiO_2$/$SiO_2$ for simultaneous photoremoval of Cr (VI) and azo dyes in a novel fixed bed continuous flow photoreactor, Canadian J. Chem. Eng. 98 (2020) 705–716.

[4] X. Li, R. Huang, Y. Hu, Y. Chen, W. Liu, R. Yuan, Z. Li, A ternplated method to $Bi_2WO_6$ hollow microspheres and their conversion to double-shell $Bi_2O_3$/$Bi_2WO_6$ hollow microspheres with improved photocatalytic performance, Inorg. Chem. 51 (2012) 6245–6250.

[5] D. Qu, L. Wang, D. Zheng, L. Xiao, B. Deng, D. Qu, An asymmetric supercapacitor with highly dispersed nano-$Bi_2O_3$ and active carbon electrodes, J. Power Sources 269 (2014) 129–135.

[6] X. Chang, G. Yu, J. Huang, Z. Li, S. Zhu, P. Yu, C. Cheng, S. Deng, G. Ji, Enhancement of photocatalytic activity over $NaBiO_3$/BiOCl composite prepared by an in situ formation strategy, Catal. Today 153 (2010) 193–199.

[7] Q. Wang, X. Shi, E. Liu, J.C. Crittenden, X. Ma, Y. Zhang, Y. Cong, Facile synthesis of AgI/BiOI-$Bi_2O_3$ multi-heterojunctions with high visible light activity for Cr(VI) reduction, J. Hazard. Mater. 317 (2016) 8–16.

[8] Y. Li, J. Wang, H. Yao, L. Dang, Z. Li, Chemical etching preparation of BiOI/$Bi_2O_3$ heterostructures with enhanced photocatalytic activities, Catal. Commun. 12 (2011) 660–664.

[9] Q. Wang, D. Jiao, J. Lian, Q. Ma, J. Yu, H. Huang, J. Zhong, J. Li, Preparation of efficient visible-light-driven BiOBr/$Bi_2O_3$ heterojunction composite with enhanced photocatalytic activities, J. Alloy. Compd. 649 (2015) 474–482.

[10] W. Gou, P. Wu, D. Jiang, X. Ma, Synthesis of AgBr/$Bi_2O_3$ composite with enhanced photocatalytic performance under visible light, J. Alloy. Compd. 646 (2015) 437–445.

[11] X. Zhang, L. Zhang, T. Xie, D. Wang, Low-temperature synthesis and high visible-light-induced photocatalytic activity of BiOI/$TiO_2$ heterostructures, J. Phys. Chem. C 113 (2009) 7371–7378.

[12] K.C. Chitrada, R. Gakhar, D. Chidambaram, E. Aston, K.S. Raja, Enhanced Performance of β-$Bi_2O_3$by In-Situ Photo-Conversion to $Bi_2O_3$-$BiO_2$-xComposite Photoanode for Solar Water Splitting, J. Electrochem. Soc. 163 (2016) H546–H558.

[13] Z. Zhang, D. Jiang, C. Xing, L. Chen, M. Chen, M. He, Novel AgI-decorated beta-$Bi_2O_3$ nanosheet heterostructured Z-scheme photocatalysts for efficient degradation of organic pollutants with enhanced performance, Dalton Trans. 44 (2015) 11582–11591.

[14] Q. Li, X. Zhao, J. Yang, C.-J. Jia, Z. Jin, W. Fan, Exploring the effects of nanocrystal facet orientations in g-$C_3N_4$/BiOCl heterostructures on photocatalytic performance, Nanoscale 7 (2015) 18971–18983.

[15] J. Zhang, W. Zhang, L. Wei, L. Pu, J. Liu, H. Liu, Y. Li, J. Fan, T. Ding, Z. Guo, Alternating multilayer structural epoxy composite coating for corrosion protection of steel, Macromol. Mater. Eng. 304 (2019) 1900374.

[16] W. Zhan, L. Sun, X. Han, Recent progress on engineering highly efficient porous semiconductor photocatalysts derived from metal–organic frameworks, Nano Micro Lett. 11 (2019) 5–32.

[17] X. Zhang, Y. Yang, W. Huang, Y. Yang, Y. Wang, C. He, N. Liu, M. Wu, L. Tang, g-$C_3N_4$/UiO-66 nanohybrids with enhanced photocatalytic activities for the oxidation of dye under visible light irradiation, Mater. Res. Bull. 99 (2018) 349–358.

[18] W. Luo, Z. Li, T. Yu, Z. Zou, Effects of surface electrochemical pretreatment on the photoelectrochemical performance of Mo-doped $BiVO_4$, J. Phys. Chem. C 116 (2012) 5076–5081.

[19] Y. Yuan, L. Yin, S. Cao, G. Xu, C. Li, C. Xue, Improving photocatalytic hydrogen production of metal-organic framework UiO-66 octahedrons by dye-sensitization, Appl. Catal. B-Environ. 168 (2015) 572–576.

[20] Y. Li, X. Shang, C. Li, X. Huang, J. Zheng, Novel p-n junction UiO-66/BiOI photocatalysts with efficient visible-light-induced photocatalytic activity, Water Sci. Technol. 77 (2018) 1441–1448.

[21] R. Peng, C.-M. Wu, J. Baltrusaitis, N.M. Dimitrijevic, T. Rajh, R.T. Koodali, Ultra-stable CdS incorporated Ti-MCM-48 mesoporous materials for efficient photocatalytic decomposition of water under visible light illumination, Chem. Commun. 49 (2013) 3221–3223.

[22] L. Shen, S. Liang, W. Wu, R. Liang, L. Wu, CdS-decorated UiO–66($NH_2$) nanocomposites fabricated by a facile photodeposition process: an efficient and stable visible-light-driven photocatalyst for selective oxidation of alcohols, J. Mater. Chem. A 1 (2013) 11473–11482.

[23] J. He, Z. Yan, J. Wang, J. Xie, L. Jiang, Y. Shi, F. Yuan, F. Yu, Y. Sun, Significantly enhanced photocatalytic hydrogen evolution under visible light over CdS embedded on metal-organic frameworks, Chem. Commun. 49 (2013) 6761–6763.

[24] E.Q. Procopio, S. Rojas, N.M. Padial, S. Galli, N. Masciocchi, F. Linares, D. Miguel, J.E. Oltra, J.A. Navarro, E. Barea, Study of the incorporation and release of the non-conventional half-sandwich ruthenium(II) metallodrug RAPTA-C on a robust MOF, Chem. Commun. 47 (2011) 11751–11753.

[25] Z. Hasan, M. Tong, B.K. Jung, I. Ahmed, C. Zhong, S.H. Jhung, Adsorption of pyridine over amino-functionalized metal-organic frameworks: attraction via hydrogen bonding versus base-base repulsion, J. Phys. Chem. C 118 (2014) 21049–21056.

[26] W.-W. Zhan, Q. Kuang, J.-Z. Zhou, X.-J. Kong, Z.-X. Xie, L.-S. Zheng, Semiconductor@Metal-organic framework core-shell heterostructures: a case of ZnO@ZIF-8 nanorods with selective photoelectrochemical response, J. Am. Chem. Soc. 135 (2013) 1926–1933.

[27] Y. Li, F. Yang, Y. Yu, Enhanced photocatalytic activity of alpha-$Bi_2O_3$ with high electron-hole mobility by codoping approach: a first-principles study, Appl. Surf. Sci. 358 (2015) 449–456.

[28] Z. Deng, X. Peng, Y.-J. Zeng, Ferrocenecarboxylic acid: a functional modulator for UiO-66 synthesis and incorporation of Pd nanoparticles, CrystEngComm 21 (2019) 1772–1779.

[29] Z. Ai, Y. Huang, S. Lee, L. Zhang, Monoclinic alpha-$Bi_2O_3$ photocatalyst for efficient removal of gaseous NO and HCHO under visible light irradiation, J. Alloy. Compd. 509 (2011) 2044–2049.

[30] M.J. Islam, H.K. Kim, D.A. Reddy, Y. Kim, T. Kim, Hierarchical BiOI nanostructures supported on a metal organic framework as efficient photocatalysts for degradation of organic pollutants in water, Dalton Trans. 46 (2017) 6013–6023.

[31] L. Han, X. Zhang, D. Wu, Construction and characterization of BiOI/NH$_2$-MIL-125 (Ti) heterostructures with excellent visible-light photocatalytic activity, J. Mater. Sci.-Mater. Electron. 30 (2019) 3773–3781.

[32] S. Sood, A. Umar, S. Kumar Mehta, S. Kumar Kansal, α-Bi$_2$O$_3$ nanorods: an efficient sunlight active photocatalyst for degradation of Rhodamine B and 2,4,6-trichlorophenol, Ceram. Int. 41 (2015) 3355–3364.

[33] K.K. Bera, R. Majumdar, M. Chakraborty, S.K. Bhattacharya, Phase control synthesis of α, β and α/β Bi$_2$O$_3$ hetero-junction with enhanced and synergistic photocatalytic activity on degradation of toxic dye, Rhodamine-B under natural sunlight, J. Hazard. Mater. 352 (2018) 182–191.

[34] X. Zhang, Y. Yang, X. Lv, Y. Wang, N. Liu, D. Chen, L. Cui, Adsorption/desorption kinetics and breakthrough of gaseous toluene for modified microporous-mesoporous UiO-66 metal organic framework, J. Hazard Mater. 366 (2019) 140–150.

[35] J.-B. Huo, L. Xu, X. Chen, Y. Zhang, J.-C.E. Yang, B. Yuan, M.-L. Fu, Direct epitaxial synthesis of magnetic Fe$_3$O$_4$@UiO-66 composite for efficient removal of arsenate from water, Microporous Mesoporous Mater. 276 (2019) 68–75.

[36] W. Zhang, Z. Yan, J. Gao, P. Tong, W. Liu, L. Zhang, Metal-organic framework UiO-66 modified magnetite@silica core-shell magnetic microspheres for magnetic solid-phase extraction of domoic acid from shellfish samples, J. Chromatogr. A 1400 (2015) 10–18.

[37] G. Huang, Z. Li, K. Liu, X. Tang, J. Huang, G. Zhang, Bismuth MOF-derived BiOBr/Bi$_{24}$O$_{31}$Br$_{10}$ heterojunctions with enhanced visible-light photocatalytic performance, Catal. Sci. Technol. 10 (2020) 4645–4654.

[38] Y. Chen, B. Zhai, Y. Liang, Y. Li, Hybrid photocatalysts using semiconductor/MOF/graphene oxide for superior photodegradation of organic pollutants under visible light, Mat. Sci. Semicon. Proc. 107 (2020) 104838.

[39] Y. Liu, S. Shen, J. Zhang, W. Zhong, X. Huang, Cu$_2$-xSe/CdS composite photocatalyst with enhanced visible light photocatalysis activity, Appl. Surf. Sci. 478 (2019) 762–769.

[40] S. Han, J. Li, K. Yang, J. Lin, Fabrication of a β-Bi$_2$O$_3$/BiOI heterojunction and its efficient photocatalysis for organic dye removal, Chin. J. Catal. 36 (2015) 2119–2126.

[41] P. Shao, S. Yu, X. Duan, L. Yang, H. Shi, L. Ding, J. Tian, L. Yang, X. Luo, S. Wang, Potential Difference Driving Electron Transfer via Defective Carbon Nanotubes toward Selective Oxidation of Organic Micropollutants, Environ. Sci. Technol. 54 (2020) 8464–8472.

[42] P. Shao, X. Duan, J. Xu, J. Tian, W. Shi, S. Gao, M. Xu, F. Cui, S.J.J.o.H.M. Wang, Heterogeneous activation of peroxymonosulfate by amorphous boron for degradation of bisphenol S, J Hazard. Mater. 322 (2017) 532–539.

[43] P. Shao, Z. Ren, J. Tian, S. Gao, X. Luo, W. Shi, B. Yan, J. Li, F. Cui, Silica hydrogel-mediated dissolution-recrystallization strategy for synthesis of ultrathin α-Fe$_2$O$_3$ nanosheets with highly exposed (110) facets: a superior photocatalyst for degradation of bisphenol S, Chem. Eng. J. 323 (2017) 64–73.

[44] Y. Li, J. Wang, H. Yao, L. Dang, Z. Li, Chemical etching preparation of BiOI/Bi$_2$O$_3$ heterostructures with enhanced photocatalytic activities, Catal. Commun. 12 (2011) 660–664.

[45] Z. Wei, N. Zheng, X. Dong, X. Zhang, H. Ma, X. Zhang, M. Xue, Green and controllable synthesis of one-dimensional Bi$_2$O$_3$/BiOI heterojunction for highly efficient visible-light-driven photocatalytic reduction of Cr(VI), Chemosphere 257 (2020) 127210.